nature microbiology

ARTICLES

https://doi.org/10.1038/s41564-020-0675-3

Check for updates

Structural insights into influenza A virus ribonucleoproteins reveal a processive helical track as transcription mechanism

Rocío Coloma[1,6], Rocío Arranz[1,6], José M. de la Rosa-Trevín[1,5], Carlos O. S. Sorzano[1], Sandie Munier[2,3,4], Diego Carlero[1], Nadia Naffakh[2,3,4], Juan Ortín[1]✉ and Jaime Martín-Benito[1]✉

The influenza virus genome consists of eight viral ribonucleoproteins (vRNPs), each consisting of a copy of the polymerase, one of the genomic RNA segments and multiple copies of the nucleoprotein arranged in a double helical conformation. vRNPs are macromolecular machines responsible for messenger RNA synthesis and genome replication, that is, the formation of progeny vRNPs. Here, we describe the structural basis of the transcription process. The mechanism, which we call the 'processive helical track', is based on the extreme flexibility of the helical part of the vRNP that permits a sliding movement between both anti-parallel nucleoprotein-RNA strands, thereby allowing the polymerase to move over the genome while bound to both RNA ends. Accordingly, we demonstrate that blocking this movement leads to inhibition of vRNP transcriptional activity. This mechanism also reveals a critical role of the nucleoprotein in maintaining the double helical structure throughout the copying process to make the RNA template accessible to the polymerase.

Influenza A virus is a causative agent of respiratory disease in humans responsible for seasonal epidemics and occasional pandemics, producing high morbidity and mortality. The viral genome contains eight single-stranded, negative-polarity viral RNA (vRNA) segments assembled into macromolecular complexes called viral ribonucleoproteins (vRNPs). Within each vRNP, the vRNA adopts a closed conformation by interaction of both ends with the viral polymerase. The rest of the RNA binds the nucleoprotein scaffold via its phosphate backbone and with a stoichiometry of around 24 nucleotides (nt) per nucleoprotein monomer[1]. The atomic structure of the nucleoprotein shows a global shape that resembles a crescent with two domains, head and body, forming a groove that is the RNA binding site[2,3]. In viral particles, the vRNPs present a highly flexible double helical structure with the polymerase at one end and a closing loop at the other[4]. The vRNPs act as molecular machines, which are responsible for the transcription and replication of the viral genome inside the nucleus of infected cells. Both functions are highly processive and mediated by the heterotrimeric polymerase complex in the vRNP context[5].

The transcription process requires coupling of the vRNP to the active cellular RNA polymerase II complex[6–9]. This is essential for the virus polymerase to gain access to newly synthesized host pre-messenger RNAs, to perform cap-snatching and hence generate the capped RNA oligonucleotides needed as primers for viral mRNA synthesis[10]. This initiation process has recently been studied in influenza B using the polymerase and a small fragment of RNA[11]. After the elongation step, transcription ends by viral polymerase stuttering at the quasi-terminal oligo(U) signal in the template, leading to polyadenylation and termination[12,13]. However, the conformation of the vRNP during the various transcription steps and the mechanism that allows transcription reinitiation on the same vRNP template remain unknown. The replication process involves unprimed initiation[14,15] and requires interaction with an additional virus polymerase complex[16,17] and soluble nucleoprotein monomers[18], resulting in the formation of a new vRNP complex containing a full-length copy of the RNA template.

In this study, we performed a detailed structural analysis of vRNPs and show the extreme conformational heterogeneity of its double helical structure. By using the inhibitor nucleozin, we show that vRNPs are highly dynamic structures and demonstrate that locking the interstrand nucleoprotein–nucleoprotein interaction blocks the transcription elongation step. Based on these results, and the imaging of in vitro transcribing vRNP intermediates, we propose a mechanism for influenza vRNP transcription, whereby the sliding of opposite vRNP strands allows the polymerase to access the entire RNA template while still bound to both 5′ and 3′ termini.

Results

Extreme structural heterogeneity in vRNP interstrand nucleoprotein–nucleoprotein interactions. Previous studies have shown the structure of full-length native[4] or recombinant[19] vRNPs, but the great flexibility of the complex[4,20] limited the resolution. In this study, using cryogenic electron microscopy (cryo-EM), we performed a detailed structural analysis of the conformational variability of vRNPs and its implication in the transcription mechanism. vRNPs were isolated from A/WSN/33 (H1N1) virions as described previously[4] and imaged on a Titan Krios microscope equipped with a Falcon II direct electron detector (Extended Data Fig. 1a). As expected, the conformational heterogeneity of the sample precluded any direct attempt at three-dimensional (3D) classification of the

[1]Centro Nacional de Biotecnología, Consejo Superior de Investigaciones Científicas (CSIC), Madrid, Spain. [2]Unité de Génétique Moléculaire des Virus à ARN, Département de Virologie, Institut Pasteur, Paris, France. [3]Centre National de la Recherche Scientifique, Unité Mixte de Recherche 3569, Paris, France. [4]Université Paris Diderot, Sorbonne Paris Cité, Paris, France. [5]Present address: Department of Biochemistry and Biophysics, Science for Life Laboratory, Stockholm University, Stockholm, Sweden. [6]These authors contributed equally: Rocío Coloma, Rocío Arranz. ✉e-mail: ortinmonton@hotmail.com; jmartinb@cnb.csic.es

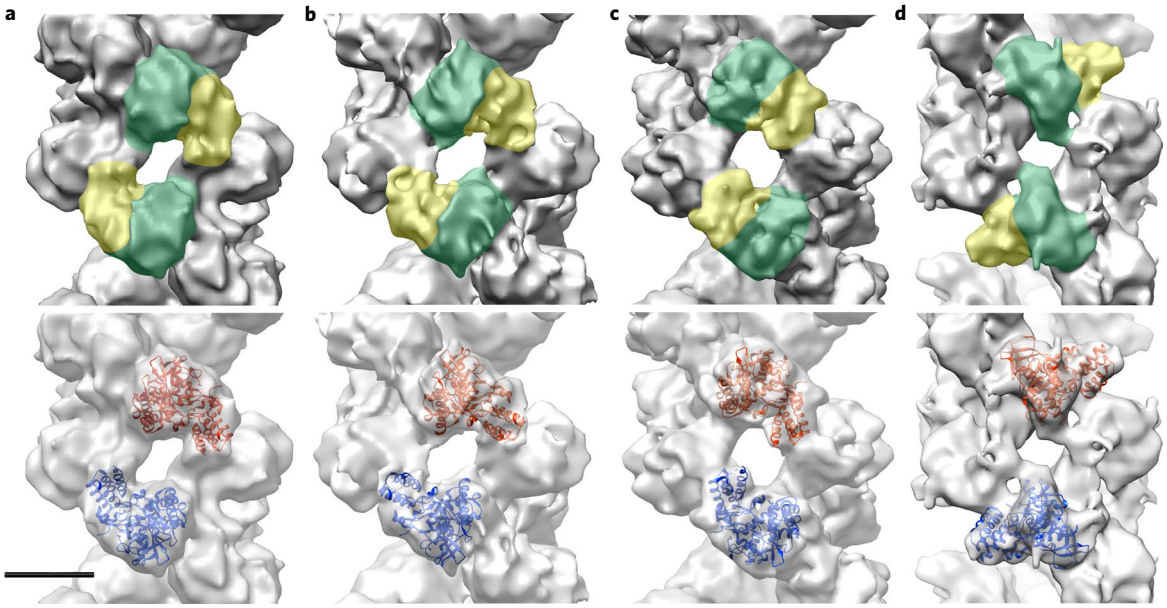

Fig. 1 | 3D reconstructions of different conformations of the helical part of vRNPs. a–d, Different conformations of the vRNP. Top row: the head and body domains of the nucleoprotein are outlined in yellow and green, respectively. Bottom row: the docking of the nucleoprotein atomic structure (PDB: 2IQH) is shown in the opposite strands in red and blue. Scale bar, 50 Å.

whole set of images applying either helical or no symmetry. To overcome this problem, we performed a two-dimensional (2D) classification using RELION software[21] to obtain groups of homogeneous images (Extended Data Fig. 1b). These groups typically contained between 1,000 and 3,000 images; the classes showing the straighter vRNP segments were selected for independent 3D reconstruction. The initial model for each class was generated using a modified version of the iterative helical real space reconstruction (IHRSR) protocol[22], where the standard programmes for search and symmetry application were replaced by others modified to deal with the heterogeneity of this sample (see Methods). After the initial model generation, structures were refined using RELION in a procedure designed ad hoc, where iterations with no symmetry alternated with iterations where helical symmetry was searched for and applied (see Methods for more information). This refinement protocol revealed that, although the structures retained the described conformation, that is, a double helical antiparallel structure with a major and a minor groove[4], there was high conformational variability in the interaction between opposing nucleoprotein-RNA strands (Fig. 1). The unambiguous docking of the nucleoprotein atomic structure[2] in the reconstructions showed that nucleoproteins in the strands could adopt a wide range of relative positions (Fig. 1 and Extended Data Figs. 2 and 3); additionally, nucleoproteins assumed different degrees of rotation relative to the strand axis (Fig. 1d and Extended Data Fig. 2d). The estimated resolution showed a global value of around 11 Å for all structures, but the local values calculated using the MonoRes programme[23] ranged from 7 to 25 Å (Fig. 2). A common characteristic to all volumes was that the RNA-binding groove region always showed the lowest resolution of the structure, pointing to the vRNA as one of the most flexible parts of the complex.

It is important to note that the images that could be used for helical reconstruction represented only a very small fraction (approximately 5%) of the vRNPs present in the micrographs. Therefore, the reconstructed structures may represent only a small portion of all possible vRNP conformations, revealing that nucleoprotein monomers can be placed in a virtually continuous distribution of relative positions on both strands, actually forming pseudohelical structures in most cases.

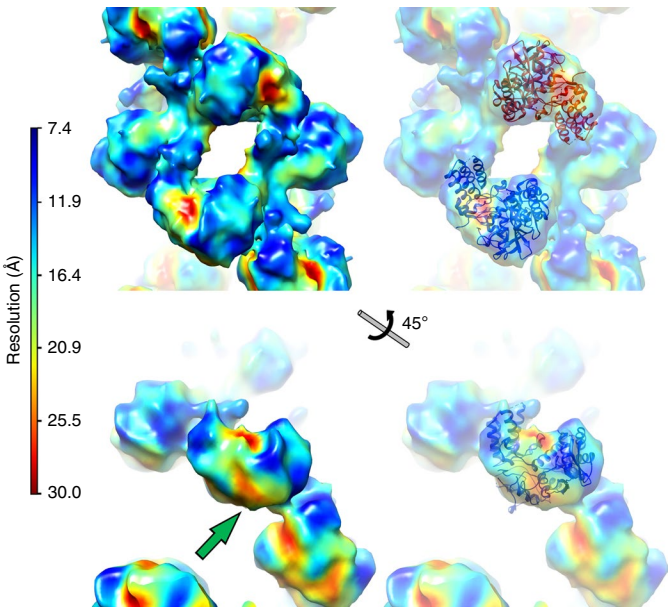

Fig. 2 | Local resolution map of vRNPs. The average resolution of the reconstructed volumes was around 11 Å in all cases, but the structures showed a wide range of resolutions in the different regions, varying from 7 to 25 Å. As an example, the resolution map of the structure shown in Fig. 1a is shown in the left column and the docking of the nucleoprotein is shown on the right. The lowest resolution corresponds to the RNA position in the binding groove of the nucleoprotein and, to a lesser extent, the region of interaction between the strands (top row). Bottom row: the external side of the nucleoprotein, also predicted to interact with RNA[4], shows a region of lower resolution (green arrow).

Highly dynamic nature of vRNP interstrand interactions. One reconstruction obtained from an underpopulated class, containing approximately 400 images, showed a structure where the nucleoprotein monomers were rotated approximately 90° from their

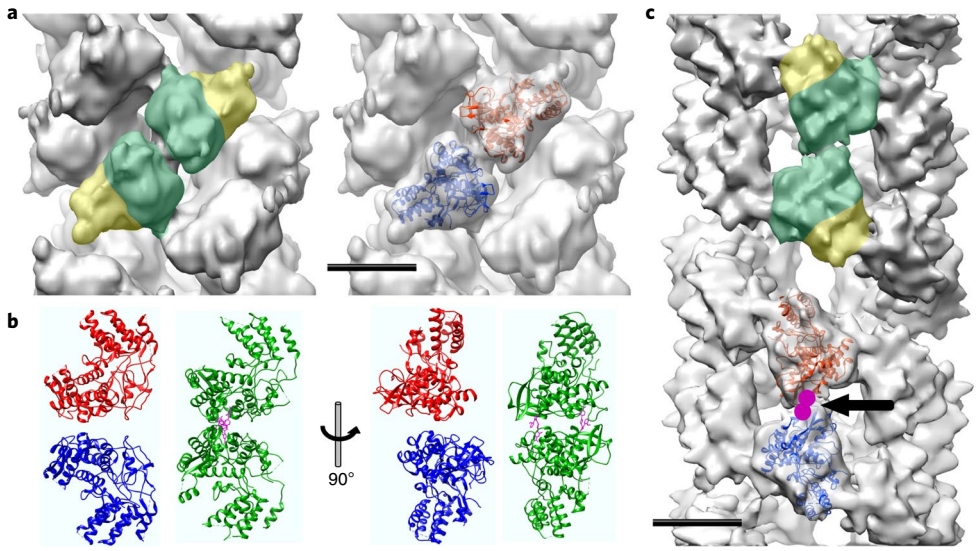

Fig. 3 | Effect of nucleozin on vRNPs structure. a, 3D reconstruction of a native vRNP showing an unusual conformation and the docking of the nucleoprotein. The nucleoproteins on the opposite strands interact through their bodies. **b**, Comparison between the relative position of the docked nucleoproteins shown in **a** (red and blue) and the nucleoprotein dimers formed on addition of a nucleozin-like inhibitor (PDB: 3RO5; green); the inhibitor is shown in magenta. **c**, One of the 3D reconstructions obtained after incubation of native vRNPs with nucleozin; treatment blocks the nucleoprotein monomers in a rotated position. The docking in the lower turn shows the contact between two nucleoproteins (black arrow); the nucleozin binding sites are shown in magenta. Scale bars, 50 Å.

usual position, that is, having the head-body axis perpendicular to the nucleoprotein-RNA strand line and contacting through the body of the molecules (Fig. 3a). Docking of the nucleoprotein atomic structure into the strands showed a structure resembling the dimers that form after treatment of free nucleoproteins with nucleozin-like inhibitors[24] (Fig. 3b). Nucleozin and nucleozin-like compounds are antiviral molecules that target nucleoprotein-dependent processes through the formation of nucleoprotein aggregates, although the actual underlying inhibitory mechanism is still unknown[24,25]. The results shown in the present study strongly suggest the possibility that nucleozin would interact directly with the native vRNPs. To study the possible conformational changes induced by these compounds, we incubated vRNPs with nucleozin and determined their structure using negative staining and cryo-EM. The characterization by negative staining showed that treated vRNPs were apparently straighter than untreated complexes (Extended Data Fig. 4a), but longer particles appeared as zigzag helices (Extended Data Fig. 4b). 2D averages of the images showed an arrangement of the helix different from the native particles and distinctive sharp corners were found along the particles (Extended Data Fig. 4c). Despite this apparent straightness, and likewise for untreated vRNPs, the cryo-EM images exhibited very high structural heterogeneity and only a small fraction of them (approximately 15%) could be used for 3D reconstruction. The final volumes showed a new helical arrangement, different from the structures obtained for untreated vRNPs, and also distinct from that obtained for the underpopulated class (Fig. 3c and Extended Data Fig. 5a). In this structure, the diameter of the helix increased substantially from around 150 to 200 Å and the nucleoprotein monomers of opposing strands were in contact at a single point on the nucleoprotein body, coinciding with one of the nucleozin binding sites as shown by the docking (Fig. 3c and Extended Data Fig. 5a). Moreover, the orientation of the nucleoprotein head-body domains indicated that the major groove of the structure had collapsed and the minor groove was opened by the action of the inhibitor (Extended Data Fig. 5b). The observation that treatment with the inhibitor resulted in straighter vRNPs while maintaining conformational variability can be explained by the 3D structures obtained. The rotation induced in the nucleoprotein monomers due to nucleozin binding decreases the head-body interaction between consecutive monomers in the same strand, which may increase the possibility of small movements and changes in the position of the nucleoprotein dimers along the *z* axis of the complex, thus maintaining structural heterogeneity (Extended Data Fig. 5c).

Nucleozin and nucleozin-like compounds act like a staple with two ends that can interact with two nucleoproteins[24]. The inhibition mechanism on vRNPs is based on the binding of one end of nucleozin to a nucleoprotein, with the other end remaining free until thermal vibration and flexibility approximates and facilitates the binding to the nucleoprotein of the adjacent turn (Extended Data Fig. 5b). After this initial union, the neighbouring nucleoproteins of contiguous turns become closer and nucleozin binding can extend cooperatively to the rest of the helix. Thus, incubation with nucleozin cross-links the nucleoproteins on opposite strands of adjacent turns and blocks the structure of the vRNP. These results also show that vRNPs are highly dynamic structures, even in the absence of any ongoing transcription or replication process.

Nucleozin treatment blocks transcription elongation in vitro. To analyse the effect of nucleozin treatment on vRNP functionality, we measured the transcriptional activity in vitro at various nucleozin concentrations (Fig. 4 and Extended Data Fig. 6). The results showed that nucleozin inhibited mRNA synthesis in a dose-dependent manner, but pretreatment time had little influence (Extended Data Fig. 6c). However, in all cases, synthesis of long fragments of mRNA was more affected than that of shorter ones. These data indicate nucleozin's ability to inhibit not only in vivo transcription activity, as reported previously[26], but also the in vitro transcription activity of isolated vRNPs, suggesting a perturbation mainly at the elongation step.

The double helical conformation is maintained during vRNP transcription. The conformational heterogeneity and flexibility of the helical part of vRNPs and the inhibition of transcription produced by cross-linking the nucleoproteins of opposite strands strongly suggests the existence of a sliding movement between both strands as a necessary step for vRNPs biological activity.

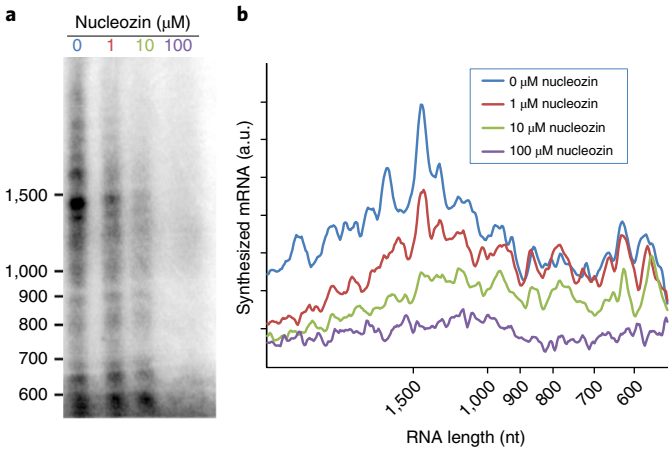

Fig. 4 | Decreased in vitro transcriptional activity of vRNPs pre-incubated with nucleozin at different concentrations. a, Gel electrophoresis of mRNA synthesized in 1 h of transcription after 60 min of incubation with different concentrations of nucleozin. **b**, Quantification of the gel shown in **a**. The decrease in RNA synthesis was much more pronounced for long mRNA transcripts, suggesting that nucleozin affects mainly the elongation process. One result from three independent experiments is shown.

To test this hypothesis, we purified vRNPs from a recombinant virus (rWSN-PB2-His_{10}) harbouring a polymerase basic protein 2 (PB2)-His-tagged polymerase, performed in vitro transcription and imaged the transcribing vRNPs by EM. Aliquots of the transcription reaction were collected at different time points, adsorbed on carbon-coated grids, negatively stained and observed on the microscope. The obtained images showed compact helical structures which maintain the double helical arrangement along practically all the vRNP, with a putative mRNA thread emerging from the middle part of the vRNP in some cases (Fig. 5a and Extended Data Fig. 7a). Also occasionally, nucleoprotein loops were visible at both ends of the vRNP (Fig. 5a and Extended Data Fig. 7a), ruling out the presence of the polymerase in any of them and indicating that it had moved to an internal point in the helical part of the complex. These particles containing two nucleoprotein loops were never observed in non-active vRNPs control preparations (summarized in Supplementary Information Table 1). Moreover, a bulky mass in the helical structure forming a discontinuity in the helix was clearly visible in most of cases. This discontinuity coincides with the point where the mRNA thread emerges and could be interpreted as the polymerase complex. To verify this hypothesis, we labelled the His-tagged PB2 subunit in activated and non-activated control vRNPs with a 5-nm Ni-NTA-Nanogold nanoprobe and they were observed under the microscope after negative staining (Fig. 5b and Extended Data Fig. 7a,b). The results showed that non-active vRNPs were labelled at one end (Extended Data Fig. 7b) in most cases (95%; Supplementary Information Table 1), depicting the expected position of the polymerase in a resting complex. The remaining 5% is probably unspecific binding to the vRNP. In contrast, the percentage of labelled complexes in the central helix region reached 35% for activated vRNPs; in these cases, the Nanogold labelling normally coincided with the mentioned discontinuity in the helical region. The remaining particles marked at one end (65%) could be interpreted as vRNPs that, despite being in the presence of the primer and nucleoside triphosphates, did not start any transcription process. These results confirmed the presence of the polymerase at an internal position in the helical region in active vRNPs.

Additionally, several images of the discontinuities containing the polymerase were selected, classified and aligned to produce more detailed averaged images of the polymerase in the helix (Fig. 5c and Extended Data Fig. 7c). In the averaged images, the presence of a large mass of approximately 100-Å diameter is clear, which could be interpreted as the polymerase (Fig. 5c, highlighted in blue) flanked by its two adjacent nucleoprotein monomers.

Discussion

The imaging of transcription intermediates indicated that vRNPs transcribe while maintaining an overall double helix structure and without unwinding the vRNP strands. Based on this and the structural analyses of vRNPs presented above, we propose a new mechanism for influenza mRNA synthesis, the 'processive helical track', where the sliding movement between the two strands allows the polymerase to move along the genomic RNA while bound to both ends (Fig. 6 and Supplementary Video). Transcription starts at the 3′ end using a host-capped mRNA as primer; then, the polymerase copies the first nucleotides of the vRNA (Fig. 6, step 1). After the 3′ end has been copied, it has been proposed that it could rebind the polymerase, a process facilitated by base pairing between the vRNA termini[27]. It is also possible that the 3′ end could rebind at some alternative site in the polymerase, as has been suggested for another segmented, negative-stranded virus, namely the La Crosse virus[28]. Subsequently, the polymerase continues copying the template and induces the movement of both strands (Fig. 6, step 2) until it reaches the poly-U region near the 5′ end. At this point, the steric hindrance caused by association of the polymerase with the 5′ end stalls the strand sliding and leads to polyadenylation of the mRNA by repetitive copying of the U tract (Fig. 6, step 3)[13,29]. Finally, the mRNA is released and the vRNP reaches the initial state (Fig. 6, step 4), allowing for a new round of transcription to begin. As shown in the Supplementary Video, it is the relative movement between the RNA-nucleoprotein strand and polymerase that allows it to move along the entire genome. It is important to stress that this mechanism does not involve sliding of the genomic RNA through the RNA-binding groove of the nucleoprotein. Rather, the template is detached from the nucleoprotein and led to the polymerization site through the entry channel present in the polymerase[27,30,31]; then, the copy process pulls the vRNA and produces the translocation of nucleoprotein towards the exit channel of the polymerase[27]. At this point, it should be noted that nucleoproteins, even in the absence of RNA, still bind each other through the tail loop present between the 402–428 amino acids[2], forming a chain as shown in the docking of the nucleoprotein in the structure of native vRNPs[4] (PDB: 4BBL). After polymerization, the template exits through the polymerase exit channel and rebinds the translocated nucleoprotein. This movement of detachment and reassembly of genomic RNA in the nucleoprotein-binding groove indicates a highly dynamic interaction, which is reflected in the low resolution presented by the vRNP structures in this region (Fig. 2).

This mechanism could also shed light on the role of the nucleoprotein during vRNP transcription. Mini-recombinant RNPs containing RNA fragments between 46 and 76 nucleotides, including the 3′ and 5′ ends of influenza, have been shown to transcribe and replicate efficiently in the absence of nucleoprotein[32,33]. Nevertheless, the presence of nucleoprotein is essential for transcription and replication of templates that are 101 nucleotides and longer, indicating that nucleoprotein acts as an elongation factor[33,34]. These data could be explained in view of the mechanism presented in this study, which provides the nucleoprotein with the ability to maintain the double helix structure of the complex during template copying, stabilizing the vRNP and keeping the vRNA in a melted and accessible conformation. In this mechanism, the nucleoproteins that flank the polymerase, that is, the nucleoproteins that directly interact with it[35], could play an important role in keeping the opposite nucleoprotein-RNA strand close to the polymerase so that the template can be maintained in the polymerase active site. In other words, the absence of nucleoprotein may lead to early release of the template, resulting in short, abortive RNA copies.

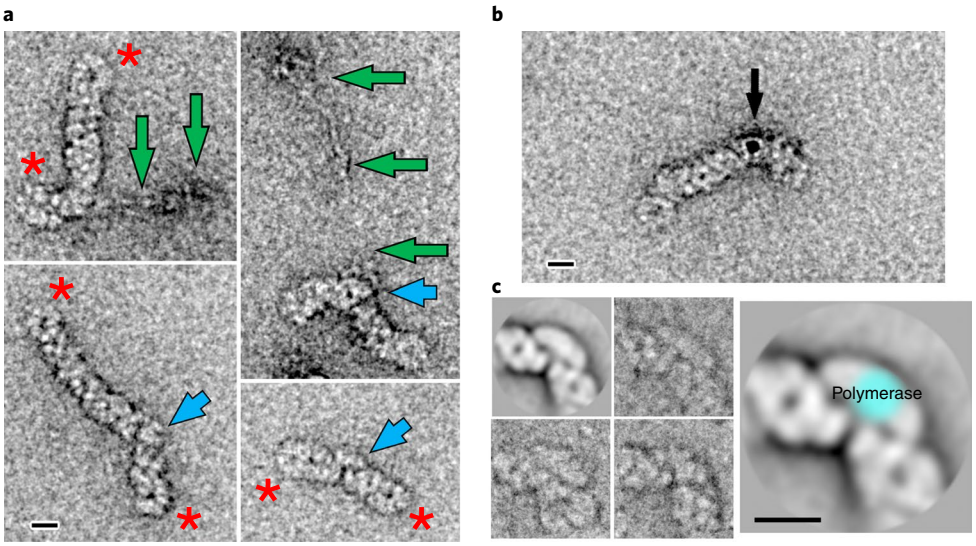

Fig. 5 | Images of the transcription process. a, Gallery of images of vRNPs during transcription. The presence of a loop at each end of the vRNPs is clear (red asterisks). The polymerase is visible as a kink in the middle of the helical part (blue arrows). In some cases, the presence of a putative nascent mRNA thread emerging from the polymerase is also evident (green arrows). **b**, Image of an active vRNP where the histidine-tagged PB2 polymerase has been labelled with a 5-nm of Ni-NTA-Nanogold nanoprobe (black arrow) to show the internal position of the polymerase. Two loops can also be seen at the ends of the vRNP. **c**, Average obtained from 234 images of the polymerase placed in the middle of the helical part of the vRNP. Representative single images of the class are shown. On the right, an interpretation of the average with the polymerase is shown in blue. Scale bars, 150 Å.

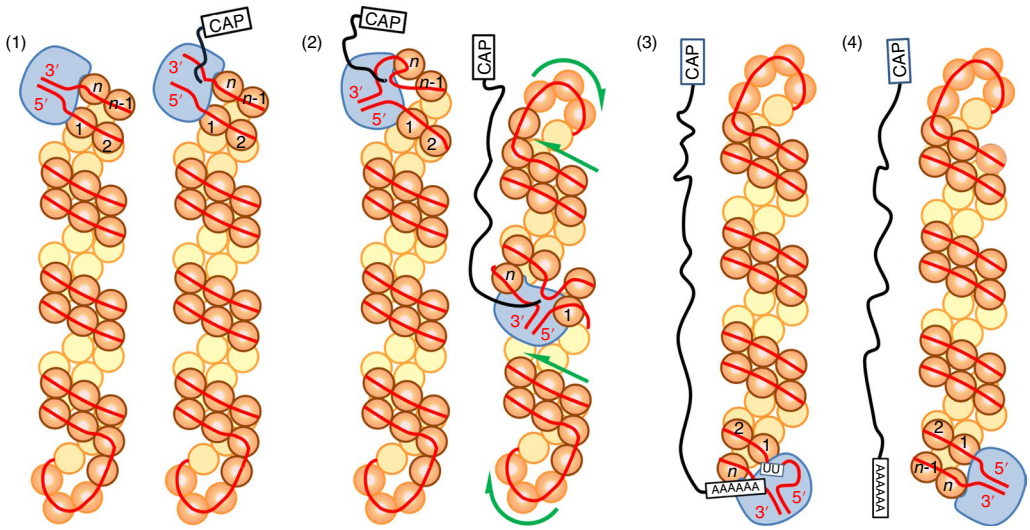

Fig. 6 | The transcription process mechanism steps. The steps are: (1) initiation; (2) elongation; (3) polyadenylation; and (4) mRNA release. Movement of the nucleoproteins is indicated by the green half-arrows (see main text and Supplementary Video for details).

The processive helical track implies that multiple interstrand nucleoprotein–nucleoprotein interactions must be broken and reformed during the elongation process. Nevertheless, we believe that the extreme flexibility of the vRNP limits the number of nucleoproteins affected simultaneously by the sliding movement, limiting the restructuring of the helical part to a local region. This idea is also supported by the fact that treatment of vRNPs with nucleozin, in the absence of any transcription or replication activity, induces a local conformation change in the vRNP that propagates sequentially until it affects the whole helix. Remarkably, this nucleozin-impelled conformational change occurs in the absence of nucleoside triphosphate hydrolysis and is driven solely by the thermal energy of the system, indicating the plasticity of nucleoprotein–nucleoprotein interactions.

Could this mechanism also be relevant in vRNP replication? Considering that nucleozin-like compounds can also inhibit in vivo replication when added late during infection[24,26], it is reasonable to think that the proposed mechanism could also play a role in genome replication, revealing possible similarities in the elongation processes during transcription and replication. Furthermore, the processive helical track mechanism would be very attractive to explain how the progeny vRNP adopts the double helix conformation during the replication process. However, confirmation or refusal of such a hypothesis must await the results of further experiments.

Methods

Biological techniques. The influenza viruses used throughout this study were A/WSN/33 (H1N1) (WSN) and a recombinant virus of the same strain, rWSN-PB2-His_{10}, which contains a C-terminal His-tagged PB2 polymerase subunit. The Madin Darby Canine Kidney (MDCK) (PTA-6500) and COS-1 (CRL-1650) cell lines were obtained from ATCC and were cultivated as described in Ortín et al.[36]. For recombinant virus production, MDCK cells were obtained from the National Reference Center for Influenza Viruses, Institut Pasteur. 293T cells were obtained from the laboratory of M. Perricaudet, Institut Gustave Roussy. Cells were not authenticated. Cells were regularly tested for the presence of *Mycoplasma* using the Myco-Alert *Mycoplasma* Detection Kit (Lonza) to ensure they were *Mycoplasma*-free.

Virus production. MDCK monolayers were infected with plaque-purified WSN virus at a multiplicity of infection (MOI) of 0.001 plaque-forming units per cell. When the cytopathogenic effect was apparent, the culture supernatant was collected and centrifuged for 10 min at 10,000*g*. Plaque assays were carried out on MDCK monolayers as described in Ortín et al.[36].

Generation of recombinant viruses by reverse genetics. A sequence encoding the polyhistidine tag (His-tag: SFLEQKLISEEDLNSA VDHHHHHHHHHH) was inserted downstream of the WSN-PB2 open reading frame in the pPolI-WSN-PB2 reverse genetics plasmid using a two-step PCR-based protocol (the sequences of the primers are available upon request). The pGEM3-Victoria-PB2-His_{10} (ref. [4]) and pPolI-WSN-PB2-SL-Luc1-143 (ref. [37]) plasmids were used as templates for the initial PCR reactions; an equimolar mixture of the overlapping PCR products was used as the template for the second PCR reaction. The resulting amplicon was cloned between the BstXI and NheI sites of pPolI-WSN-PB2-SL-Luc1-143, forming pPolI-WSN-PB2-His-143, where the His-tag is followed by a stop codon and a duplication of the 5′-terminal 143 nt of the PB2 segment that ensures integrity of the packaging signals present at the 5′ end.

The method used to produce the recombinant rWSN-PB2-His_{10} virus by reverse genetics was adapted from procedures described previously[38]. Briefly, the 8 pPolI-WSN and 4 pcDNA3.1-WSN plasmids (0.5 µg for each) were cotransfected into a subconfluent monolayer of cocultivated 293T and MDCK cells (4×10^5 and 3×10^5 cells, respectively, seeded in a 35-mm dish) using 10 µl of FuGENE HD transfection reagent (Promega Corporation). After 24 h of incubation at 35 °C, the supernatant was removed and cells were washed twice with DMEM and incubated at 35 °C in DMEM containing tosyl phenylalanyl chloromethyl ketone (TPCK)-treated trypsin (Worthington) at a final concentration of 1 µg ml^{-1} for 48 h. The efficiency of reverse genetics was evaluated by titrating the supernatant by plaque assay on MDCK cells[39]. For subsequent viral amplification, MDCK cells were infected at an MOI = 0.001 and incubated for 3 d at 35 °C in DMEM containing TPCK-treated trypsin at a concentration of 1 µg ml^{-1}. The viral stock was titrated by plaque assay on MDCK cells and viral RNA was sequenced after reverse transcription–PCR amplification.

Virus purification. For virus purification, clarified virus supernatants were centrifuged over a 33% sucrose cushion in TNE buffer (50 mM of Tris-HCl, 150 mM of KCl, 0.1 mM of EDTA at pH 7.4) for 2.5 h at 25,000 r.p.m. and 4 °C in an SW 28 Ti swinging-bucket aluminum rotor (Beckman Coulter).

vRNP purification. Purified virions were disrupted as described by Parvin et al.[40] and vRNPs were purified by centrifugation on a 15–30% glycerol gradient in TN buffer (50 mM of Tris-HCl, 150 mM of KCl) as described previously by Compans et al.[41]. vRNPs from rWSN-PB2-His_{10} virions were purified by centrifugation on a 15–30% glycerol gradient in TN buffer. The concentration of purified vRNPs was determined by western blot using antibodies specific for nucleoprotein and the PA subunit of the polymerase. Finally, vRNP activity was checked by in vitro RNA synthesis as described by Coloma et al.[35], using either β-globin mRNA or ApG as primers.

Transcription assays in the presence of nucleozin. To determine the transcriptional activity of purified vRNPs in the presence of nucleozin (Merck Millipore)[25], samples were first pre-incubated in a buffer containing 50 mM of Tris-HCl, 5 mM of $MgCl_2$, 100 mM of KCl, 1 mM of dithiothreitol (DTT) and 0, 1, 10 or 100 µM of nucleozin for 10 or 60 min at 30 °C. After nucleozin treatment, samples were supplemented with 10 mg ml^{-1} of actinomycin D, 1 U µl^{-1} of RNasin, 1 mM of ATP, 1 mM of cytidine triphosphate (CTP), 1 mM of uridine-5′-triphosphate (UTP), 1 µM of guanosine triphosphate (GTP), 10 µCi of αP^{32}-GTP (3,000 Ci mmol^{-1}) and 100 µM of ApG, and incubated for 1 h at 30 °C (ref. [35]). To analyse the transcription products, synthesized RNA was isolated by treatment with proteinase K (50 mg ml^{-1}) for 30 min at 37 °C in TNE buffer, 1% SDS and extracted with phenol. The RNA was ethanol-precipitated, resuspended in formamide loading buffer and analysed by denaturing gel electrophoresis[35].

Effect of nucleozin on the 3D structure of vRNPs. To analyse the structure of vRNPs after incubation with nucleozin, purified vRNPs were incubated in a buffer containing 50 mM of Tris-HCl, 5 mM of $MgCl_2$, 100 mM of KCl, 1 mM of DTT and 1 or 100 µM nucleozin for 60 min at 30 °C. After treatment, samples were used for EM analysis.

Transcriptional intermediates. To analyse the structure of vRNPs during in vitro transcription, His-tagged vRNPs purified on glycerol gradients were incubated in a buffer containing 50 mM of Tris-HCl, pH 7.5, 5 mM of $MgCl_2$, 100 mM of KCl, 1 mM of DTT, 10 mg ml^{-1} of actinomycin D, 1 U µl^{-1} of RNasin, 1 mM of ATP, 1 mM of CTP, 1 mM of UTP, 1 mM of GTP and 10 µg ml^{-1} mRNA β-globin at 30 °C. Reactions were stopped at 5, 15 and 60 min and used to prepare EM grids.

Nanogold labelling of the polymerase in transcriptional intermediates was performed as follows: reactions prepared as described earlier were incubated with 5-nm of Ni-NTA-Nanogold (Nanoprobes) 1:5 (v/v) for 1 h at 4 °C, after which grids were prepared for EM.

EM and image processing. *vRNP cryo-EM and 3D reconstruction.* For cryo-EM, between 3 and 5 µl aliquots of purified vRNPs were applied to glow-discharged, carbon-coated Cu/Rh 300 mesh Quantifoil R 2/2 µm holey grids (Quantifoil Micro Tools) for 5 min, blotted for 2 s and frozen in liquid ethane using a Leica EM CPC cryo-fixation unit (Leica Microsystems). The vitrified grids were transferred onto a Titan Krios transmission electron microscope (Thermo Fisher Scientific) and images were recorded on a Falcon II direct electron detector (Thermo Fisher Scientific). A total of 420 movies with 69 frames and defocus ranging from 1.5 to 3.0 µm were collected with a sampling ratio of 2.26 Å per pixel (px).

Most of the image handling and processing protocols were performed within the Scipion software suite (v.1.2)[42] (http://scipion.i2pc.es/). Movies were imported into Scipion and corrected for beam-induced movement using either the optical flow approach[43] or MotionCorr software (v.2.1)[44]. The contrast transfer function (CTF) parameters of the aligned movies were determined using the CTFFIND software (v.4.1.1)[45]. To reconstruct the vRNPs, a total of 137,461 images of the straighter particles were manually selected from the micrographs, representing approximately a quarter of the total number of complexes present in the images. In the first step, 200 × 200-px images of the helical segments were extracted and vertically pre-aligned using a multi-reference, pattern-free alignment protocol[46]. After this pre-alignment, images were cropped to 120 × 120 px and subjected to 2D classification using the RELION software (v.2.0)[21] (https://www2.mrc-lmb.cam.ac.uk/relion). This classification allowed us to identify the straightest particles and obtain homogeneous groups of vRNPs images that could be used for 3D reconstruction. The groups typically contained between 1,000 and 4,000 images and were reconstructed independently. For each group, an initial helical model was built using a modified version of the IHRSR[22] in the Spider software (v.18.0)[47]. The protocol was broadly the same as described by Egelman[22], except that the programmes for helical search symmetry (HSEARCH) and symmetry imposition (HIMPOSE) were replaced by two custom-made programmes prepared for this study, namely xmipp_find_symmetry and xmipp_symmetrize, implemented in the XMIPP software (v.3.0)[48]. The initial helical parameters were taken from our previous data[4]. After generating the starting model for each class, a refinement was performed using a protocol designed to deal with the extreme flexibility of the vRNPs. The protocol was an iterative refinement where several rounds of refinement without any symmetry imposition were alternated with rounds where helical symmetry was searched for and applied.

With some variation, depending on the characteristics of the group of images under study, the refinement followed the following general scheme: the initial model obtained with the IHRSR protocol was filtered at approximately 65 Å and was followed by a refinement using RELION with no symmetry imposition (c1); every 4–5 iterations, helical symmetry was searched for and applied to the output volume using the aforementioned XMIPP programmes and a new round of iterations with no symmetry was performed. The refinement radius was around 200–220 Å, depending on the straightness of the particles; the radius for symmetry search was around 60–80% of the refinement radius. These refinement steps were repeated until the angular assignment of the images and resolution did not change. After this, a new round of alternate refinements in c1 and with symmetry was carried out; however, in this second stage, the refinement radius was linearly reduced and so was the number of iterations without symmetry depending on the variation of the symmetry parameters. When the symmetry parameters were stable, symmetry was applied in all rounds until the angular assignment and resolution did not change. The final resolution of the reconstructed volumes was calculated using the MonoRes software[23] implemented in Scipion.

Characterization of nucleozin-treated vRNPs and 3D reconstruction. For nucleozin-treated vRNPs, an initial characterization was performed using negative staining methods. Briefly, aliquots of 10 µl of vRNPs pre-treated with 1 or 100 µM nucleozin for 1 h were adsorbed on glow-discharged Cu/Rh 200-mesh carbon-coated grids for 2 min and stained with uranyl acetate 2% (w/v) for 2 min. Grids were inspected in a JEOL 1200EX II (Japan Electron Optics Laboratory). Samples treated with 100 µM nucleozin showed a higher level of vRNP aggregation and were discarded. Then, the grids of vRNPs treated with 1 µM nucleozin were selected for in-depth characterization either by negative staining or cryo-EM for 3D reconstruction.

The selected negatively stained grids were transferred onto a FEI Tecnai G2 F20 electron microscope operated at 200 KV (Thermo Fisher Scientific); 367 images

were recorded following low-dose protocols on an Eagle 4k CCD camera (Thermo Fisher Scientific) using serial EM software (v.3.6.0 beta)[49] at a sampling ratio of 2.16 Å per px. The images were imported into Scipion and the CTF was calculated using CTFFIND. To study the characteristic bending of nucleozin-treated vRNPs, 1,648 of these kinks were manually selected, extracted in 250 × 250-px boxes and classified using RELION. This processing produced homogeneous classes with around 150–250 images per class, showing a typical central line and the striking bends of this sample.

Negatively stained images were also used to obtain the initial 3D model of nucleozin-treated vRNPs. For this purpose, 7,489 images were manually selected from the straightest segments and extracted in 140 × 140-px boxes. The images were vertically pre-aligned as described earlier and then classified using RELION. The best segments were selected to find the helical symmetry parameters as described by Arranz et al.[4], and the results were used as the initial model for the cryo-EM 3D reconstruction.

For cryo-EM, 5 µl aliquots of 1 µM nucleozin-treated vRNPs were applied to glow-discharged carbon-coated Cu/Rh 300-mesh Quantifoil R 2/2 µm holey grids for 5 min, blotted for 2 s and frozen in liquid ethane using a Leica EM CPC cryo-fixation unit. The vitrified grids were transferred onto a Talos Arctica transmission electron microscope (Thermo Fisher Scientific) and images were recorded on a Falcon II direct electron detector. A total of 1,029 movies with 21 frames and defocus ranging from 1.5 to 3.0 µm were collected at a sampling ratio of 1.41 Å per px. The movies were imported into the Scipion software to correct beam-induced movements, find the CTF parameters, select the particles and extract the images. In this case, 33,037 images were manually selected from the micrographs and 3D-reconstructed following a protocol like that described for the untreated vRNPs.

vRNP transcription intermediates. For conventional negative stain EM of the transcription process, 5 µl aliquots of vRNPs prepared as described in the Biological Techniques section were applied to glow-discharged, carbon-coated grids for 5 min. Samples were washed three times and stained for 1 min with uranyl acetate 2% (w/v). Grids were transferred to a FEI Tecnai G2 F20 electron microscope operated at 200 KV using a side-entry holder. Images were recorded using serial EM software on an Eagle 4k CCD camera following low-dose protocols at a sampling ratio of 1.8 Å per px and defocus ranging from 1.5 to 3.5 µm.

For transcription analysis, 5,446 images were acquired and processed in Scipion using the guidelines described earlier. From these images, 2,387 particles containing the polymerase somewhere in the helical part were manually selected, extracted in 256 × 256-px boxes and classified using RELION. Finally, gels were quantified using the ImageJ software (v.1.42g)[50] (https://imagej.net/); all molecular graphics and figures were generated with the UCSF Chimera package (v.1.11)[51] (http://www.rbvi.ucsf.edu/chimera).

Reporting Summary. Further information on research design is available in the Nature Research Reporting Summary linked to this article.

Data availability

The EM maps have been deposited with the Electron Microscopy Data Bank (https://www.ebi.ac.uk/pdbe/emdb) under accession numbers EMD-0175, EMD-4412, EMD-4423, EMD-4426 and EMD-4430. The atomic coordinates of the docking have been deposited with the Protein Data Bank (https://www.rcsb.org/) under accession numbers 6H9G, 6I54, 6I7B, 6I7M and 6I85.

Received: 19 October 2018; Accepted: 24 January 2020;
Published online: 9 March 2020

References

1. Ortega, J. et al. Ultrastructural and functional analyses of recombinant influenza virus ribonucleoproteins suggest dimerization of nucleoprotein during virus amplification. *J. Virol.* **74**, 156–163 (2000).
2. Ye, Q., Krug, R. M. & Tao, Y. J. The mechanism by which influenza A virus nucleoprotein forms oligomers and binds RNA. *Nature* **444**, 1078–1082 (2006).
3. Ng, A. K. et al. Structure of the influenza virus A H5N1 nucleoprotein: implications for RNA binding, oligomerization, and vaccine design. *FASEB J.* **22**, 3638–3647 (2008).
4. Arranz, R. et al. The structure of native influenza virion ribonucleoproteins. *Science* **338**, 1634–1637 (2012).
5. Eisfeld, A. J., Neumann, G. & Kawaoka, Y. At the centre: influenza A virus ribonucleoproteins. *Nat. Rev. Microbiol.* **13**, 28–41 (2015).
6. Engelhardt, O. G., Smith, M. & Fodor, E. Association of the influenza A virus RNA-dependent RNA polymerase with cellular RNA polymerase II. *J. Virol.* **79**, 5812–5818 (2005).
7. Lukarska, M. et al. Structural basis of an essential interaction between influenza polymerase and Pol II CTD. *Nature* **541**, 117–121 (2017).
8. Rodriguez, A., Pérez-González, A. & Nieto, A. Influenza virus infection causes specific degradation of the largest subunit of cellular RNA polymerase II. *J. Virol.* **81**, 5315–5324 (2007).
9. Serna Martin, I. et al. A mechanism for the activation of the influenza virus transcriptase. *Mol. Cell* **70**, 1101–1110 (2018).
10. Bouloy, M., Plotch, S. J. & Krug, R. M. Globin mRNAs are primers for the transcription of influenza viral RNA in vitro. *Proc. Natl Acad. Sci. USA* **75**, 4886–4890 (1978).
11. Kouba, T., Drncová, P. & Cusack, S. Structural snapshots of actively transcribing influenza polymerase. *Nat. Struct. Mol. Biol.* **26**, 460–470 (2019).
12. Li, X. & Palese, P. Characterization of the polyadenylation signal of influenza virus RNA. *J. Virol.* **68**, 1245–1249 (1994).
13. Robertson, J. S., Schubert, M. & Lazzarini, R. A. Polyadenylation sites for influenza virus mRNA. *J. Virol.* **38**, 157–163 (1981).
14. Hay, A. J., Skehel, J. J. & McCauley, J. Structure and synthesis of influenza virus complementary RNAs. *Phil. Trans. R. Soc. Lond. B* **288**, 341–348 (1980).
15. Vreede, F. T. & Brownlee, G. G. Influenza virion-derived viral ribonucleoproteins synthesize both mRNA and cRNA in vitro. *J. Virol.* **81**, 2196–2204 (2007).
16. Jorba, N., Coloma, R. & Ortín, J. Genetic trans-complementation establishes a new model for influenza virus RNA transcription and replication. *PLoS Pathog.* **5**, e1000462 (2009).
17. York, A., Hengrung, N., Vreede, F. T., Huiskonen, J. T. & Fodor, E. Isolation and characterization of the positive-sense replicative intermediate of a negative-strand RNA virus. *Proc. Natl Acad. Sci. USA* **110**, E4238–E4245 (2013).
18. Huang, T. S., Palese, P. & Krystal, M. Determination of influenza virus proteins required for genome replication. *J. Virol.* **64**, 5669–5673 (1990).
19. Moeller, A., Kirchdoerfer, R. N., Potter, C. S., Carragher, B. & Wilson, I. A. Organization of the influenza virus replication machinery. *Science* **338**, 1631–1634 (2012).
20. Gallagher, J. R., Torian, U., McCraw, D. M. & Harris, A. K. Structural studies of influenza virus RNPs by electron microscopy indicate molecular contortions within NP supra-structures. *J. Struct. Biol.* **197**, 294–307 (2017).
21. Scheres, S. H. W. RELION: implementation of a Bayesian approach to cryo-EM structure determination. *J. Struct. Biol.* **180**, 519–530 (2012).
22. Egelman, E. H. A robust algorithm for the reconstruction of helical filaments using single-particle methods. *Ultramicroscopy* **85**, 225–234 (2000).
23. Vilas, J. L. et al. MonoRes: automatic and accurate estimation of local resolution for electron microscopy maps. *Structure* **26**, 337–344 (2018).
24. Gerritz, S. W. et al. Inhibition of influenza virus replication via small molecules that induce the formation of higher-order nucleoprotein oligomers. *Proc. Natl Acad. Sci. USA* **108**, 15366–15371 (2011).
25. Kao, R. Y. et al. Identification of influenza A nucleoprotein as an antiviral target. *Nat. Biotechnol.* **28**, 600–605 (2010).
26. Amorim, M. J., Kao, R. Y. & Digard, P. Nucleozin targets cytoplasmic trafficking of viral ribonucleoprotein-Rab11 complexes in influenza A virus infection. *J. Virol.* **87**, 4694–4703 (2013).
27. Te Velthuis, A. J. & Fodor, E. Influenza virus RNA polymerase: insights into the mechanisms of viral RNA synthesis. *Nat. Rev. Microbiol.* **14**, 479–493 (2016).
28. Gerlach, P., Malet, H., Cusack, S. & Reguera, J. Structural insights into bunyavirus replication and its regulation by the vRNA promoter. *Cell* **161**, 1267–1279 (2015).
29. Luo, G. X., Luytjes, W., Enami, M. & Palese, P. The polyadenylation signal of influenza virus RNA involves a stretch of uridines followed by the RNA duplex of the panhandle structure. *J. Virol.* **65**, 2861–2867 (1991).
30. Pflug, A., Guilligay, D., Reich, S. & Cusack, S. Structure of influenza A polymerase bound to the viral RNA promoter. *Nature* **516**, 355–360 (2014).
31. Reich, S. et al. Structural insight into cap-snatching and RNA synthesis by influenza polymerase. *Nature* **516**, 361–366 (2014).
32. Resa-Infante, P., Recuero-Checa, M. A., Zamarreño, N., Llorca, O. & Ortín, J. Structural and functional characterization of an influenza virus RNA polymerase-genomic RNA complex. *J. Virol.* **84**, 10477–10487 (2010).
33. Turrell, L., Lyall, J. W., Tiley, L. S., Fodor, E. & Vreede, F. T. The role and assembly mechanism of nucleoprotein in influenza A virus ribonucleoprotein complexes. *Nat. Commun.* **4**, 1591 (2013).
34. Honda, A., Uéda, K., Nagata, K. & Ishihama, A. RNA polymerase of influenza virus: role of NP in RNA chain elongation. *J. Biochem.* **104**, 1021–1026 (1988).
35. Coloma, R. et al. The structure of a biologically active influenza virus ribonucleoprotein complex. *PLoS Pathog.* **5**, e1000491 (2009).
36. Ortín, J., Nájera, R., López, C., Dávila, M. & Domingo, E. Genetic variability of Hong Kong (H3N2) influenza viruses: spontaneous mutations and their location in the viral genome. *Gene* **11**, 319–331 (1980).
37. Munier, S., Rolland, T., Diot, C., Jacob, Y. & Naffakh, N. Exploration of binary virus–host interactions using an infectious protein complementation assay. *Mol. Cell. Proteomics* **12**, 2845–2855 (2013).
38. Fodor, E. et al. Rescue of influenza A virus from recombinant DNA. *J. Virol.* **73**, 9679–9682 (1999).
39. Matrosovich, M., Matrosovich, T., Garten, W. & Klenk, H-D. New low-viscosity overlay medium for viral plaque assays. *Virol. J.* **3**, 63 (2006).
40. Parvin, J. D., Palese, P., Honda, A., Ishihama, A. & Krystal, M. Promoter analysis of influenza virus RNA polymerase. *J. Virol.* **63**, 5142–5152 (1989).

41. Compans, R. W., Content, J. & Duesberg, P. H. Structure of the ribonucleoprotein of influenza virus. *J. Virol.* **10**, 795–800 (1972).
42. de la Rosa-Trevín, J. M. et al. Scipion: a software framework toward integration, reproducibility and validation in 3D electron microscopy. *J. Struct. Biol.* **195**, 93–99 (2016).
43. Abrishami, V. et al. Alignment of direct detection device micrographs using a robust Optical Flow approach. *J. Struct. Biol.* **189**, 163–176 (2015).
44. Li, X. et al. Electron counting and beam-induced motion correction enable near-atomic-resolution single-particle cryo-EM. *Nat. Methods* **10**, 584–590 (2013).
45. Mindell, J. A. & Grigorieff, N. Accurate determination of local defocus and specimen tilt in electron microscopy. *J. Struct. Biol.* **142**, 334–347 (2003).
46. Sorzano, C. O. et al. A clustering approach to multireference alignment of single-particle projections in electron microscopy. *J. Struct. Biol.* **171**, 197–206 (2010).
47. Shaikh, T. R. et al. SPIDER image processing for single-particle reconstruction of biological macromolecules from electron micrographs. *Nat. Protoc.* **3**, 1941–1974 (2008).
48. de la Rosa-Trevín, J. M. et al. Xmipp 3.0: an improved software suite for image processing in electron microscopy. *J. Struct. Biol.* **184**, 321–328 (2013).
49. Mastronarde, D. N. Automated electron microscope tomography using robust prediction of specimen movements. *J. Struct. Biol.* **152**, 36–51 (2005).
50. Schneider, C. A., Rasband, W. S. & Eliceiri, K. W. NIH Image to ImageJ: 25 years of image analysis. *Nat. Methods* **9**, 671–675 (2012).
51. Pettersen, E. F. et al. UCSF Chimera—a visualization system for exploratory research and analysis. *J. Comput. Chem.* **25**, 1605–1612 (2004).

Acknowledgements

We thank S.H.W. Scheres, C. Savva and the Laboratory of Molecular Biology (Cambridge) for access to the Titan Krios microscope and technical assistance. We thank E. Sahagún for the generation of the Supplementary video (https://scixel.es/). The professional editing service NB Revisions (https://www.nbrevisions.com/) was used for technical editing of the manuscript before submission. We acknowledge the cryo-EM facility of the CNB–CIB (CSIC) for its technical advice and support throughout this work. This work was supported by the Spanish Ministry of Science, Innovation and Universities (Ministerio de Ciencia, Innovación y Universidades) grant nos. BFU2017-90018-R and BFU2011-25090/BMC (J.M.-B.) and Integrative Biology of Emerging Infectious Diseases LabEx grant no. 10-LABX-0062 (N.N.).

Author contributions

J.M.-B. and J.O. designed the experiments. R.C., R.A., D.C. and J.M.-B. carried out the experiments. J.M.R-T. and C.O.S.S. contributed the analysis tools. S.M. and N.N. contributed materials. R.C., R.A., J.O. and J.M.-B. analysed the data. J.M.-B. wrote the paper with contributions from all the other authors.

Competing interests

The authors declare no competing interests.

Additional information

Extended data is available for this paper at https://doi.org/10.1038/s41564-020-0675-3.

Supplementary information is available for this paper at https://doi.org/10.1038/s41564-020-0675-3.

Correspondence and requests for materials should be addressed to J.O. or J.M.-B.

Reprints and permissions information is available at www.nature.com/reprints.

Publisher's note Springer Nature remains neutral with regard to jurisdictional claims in published maps and institutional affiliations.

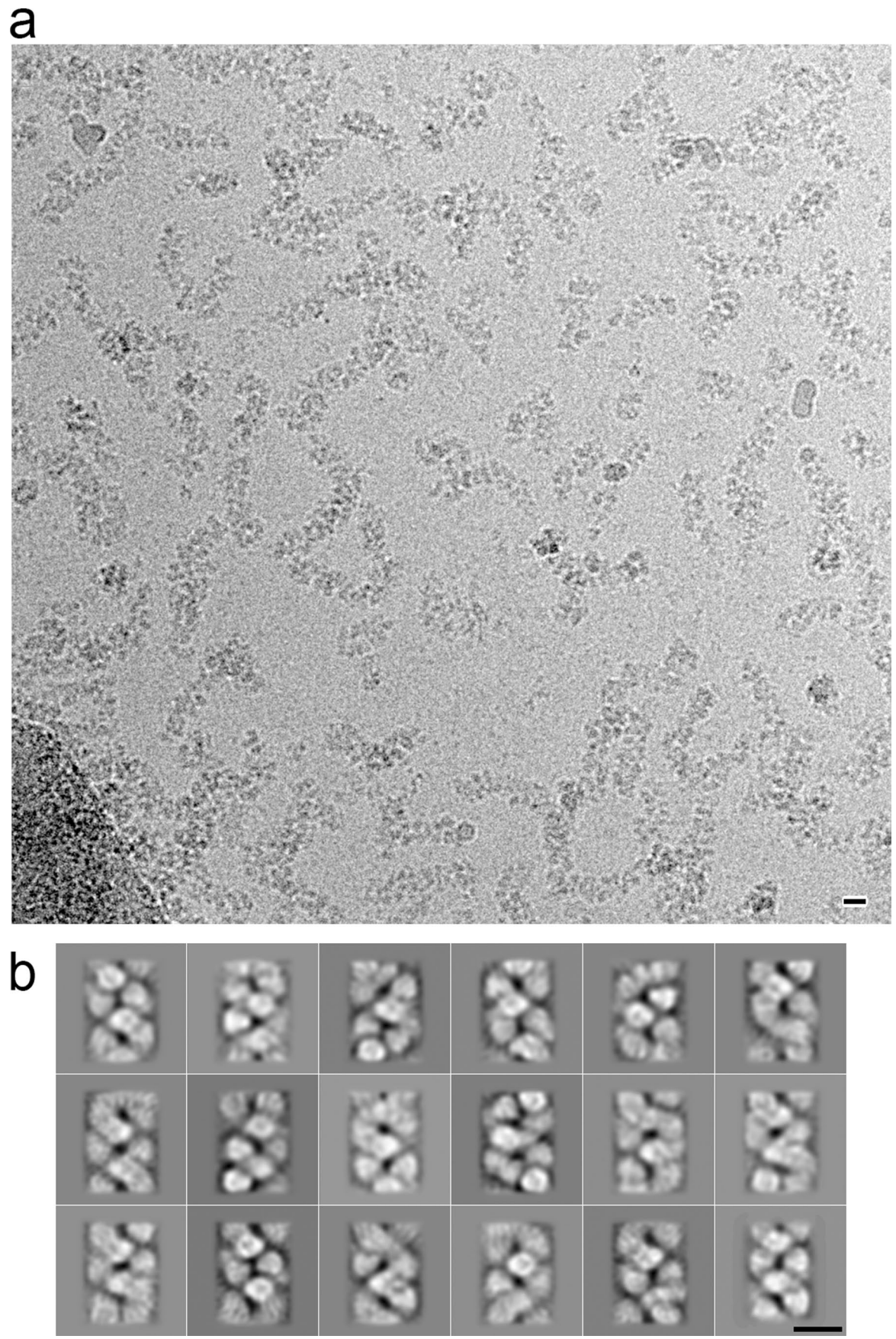

Extended Data Fig. 1 | Cryo-EM of wild type vRNPs. a, Cryo-EM image of isolated vRNPs showing the extreme flexibility of the particles. **b**, Gallery of 2D averages with some examples of the different structures of the helical part of influenza vRNPs. Scale bars represent 100Å.

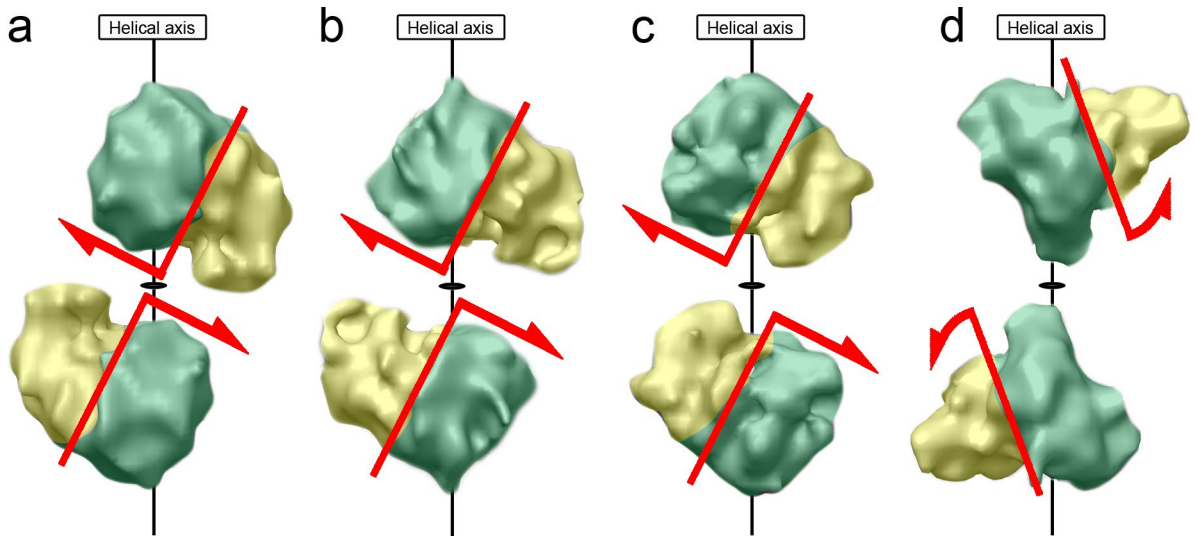

Extended Data Fig. 2 | Variation of the relative position of two nucleoprotein monomers extracted from opposite strands of the helixes shown in Fig. 1 a-d of the main text. For clarity, the equatorial region between the head (yellow) and body (green) domains has been marked with a red line, with the arrows indicating the direction of displacement. In all cases the position of the helical axis of the vRNP is represented with a vertical black line and the position of the dihedral axis is perpendicular to the plane of the figure and depicted by the (⬬) symbol.

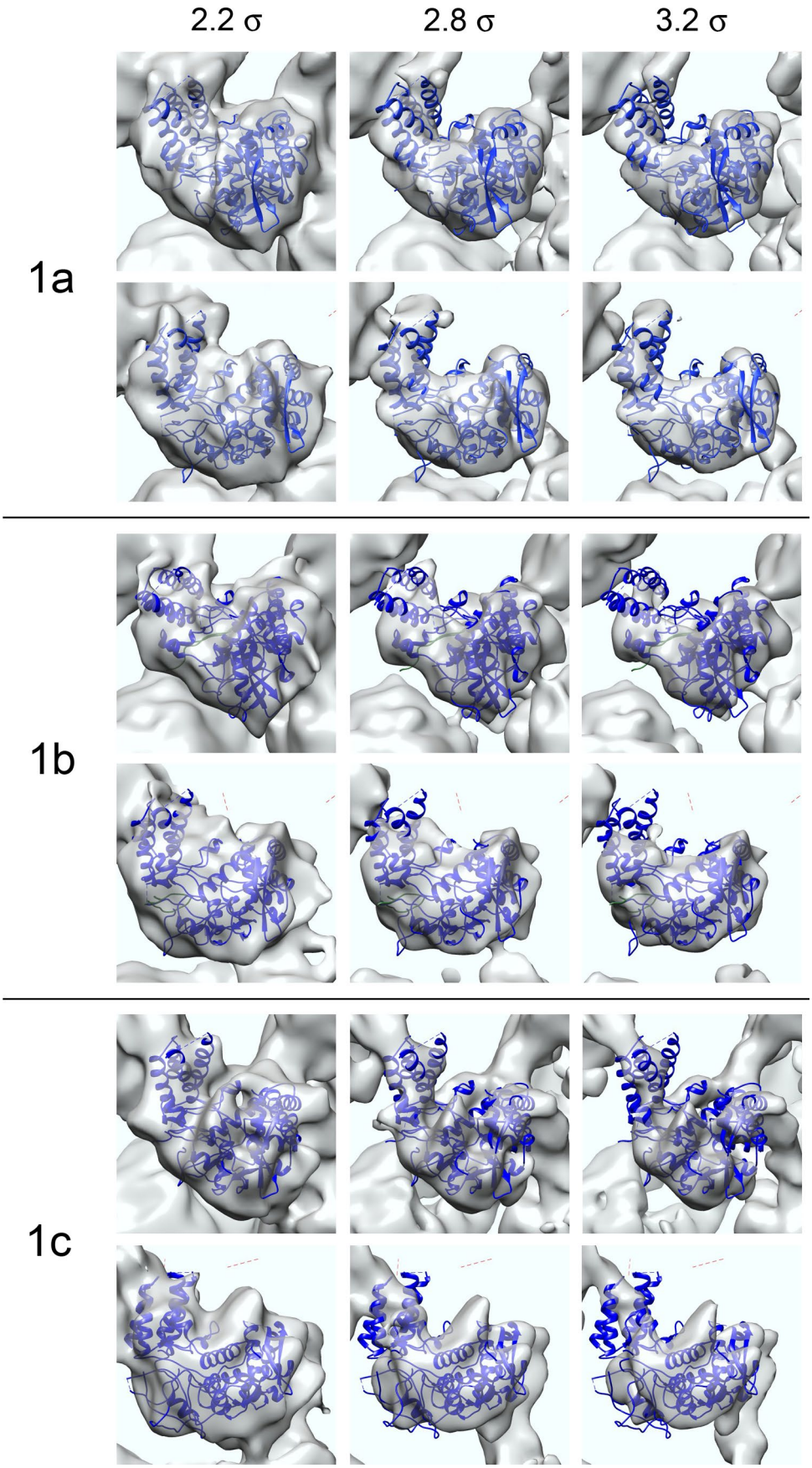

Extended Data Fig. 3 | See next page for caption.

Extended Data Fig. 3 | Docking reliability of the nucleoprotein atomic structure (pdb 2IQH) into the cryo-EM density maps. From top to bottom, six views representing two rotated positions (top and bottom raw for each case) of the cryo-EM density maps shown at three different thresholds (2.2, 2.8 and 3.2 σ) corresponding to the volumes shown in Fig. 1a–c, respectively. It is important to notice that cryo-EM maps contain the genomic ARN not present in the atomic structure. In all cases, the quality of the fit of the nucleoprotein atomic structure into the map is evident.

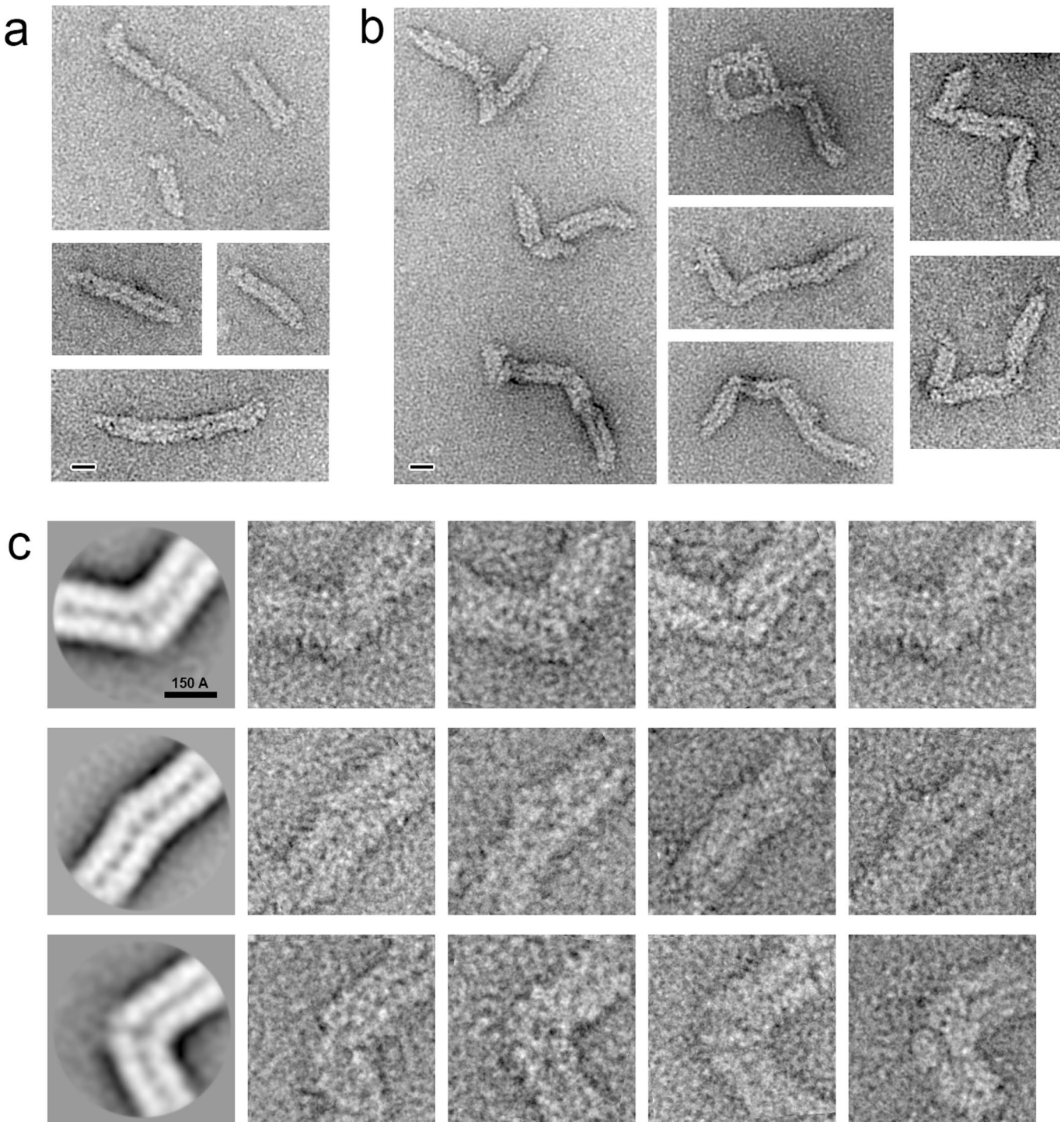

Extended Data Fig. 4 | Negative staining electron microscopy characterization of nucleozin-treated vRNPs. a, After nucleozin treatment, vRNPs appear as straight structures with a characteristic dark centerline along the helix. **b**, Longer vRNPs appear as broken helixes showing sharp corners. These structures probably formed from the initial binding of nucleozin at different points of one long helix followed by a cooperative extension of the conformational change induced by the drug; the growth of the straight segments generates these striking bends in the joint zones (see Extended Data Fig. 5 for more information). **c**, Gallery of averaged kinks selected from the nucleozin-treated vRNPs. The treated particles always show a characteristic central line and an increase in the diameter of the helix is clearly visible (compare with Extended Data Fig. 1b), indicating that a conformational change has occurred. Representative individual images of each class are shown on the right. Scale bar represents 200 Å in **a** and **b** and 150 Å in **c**.

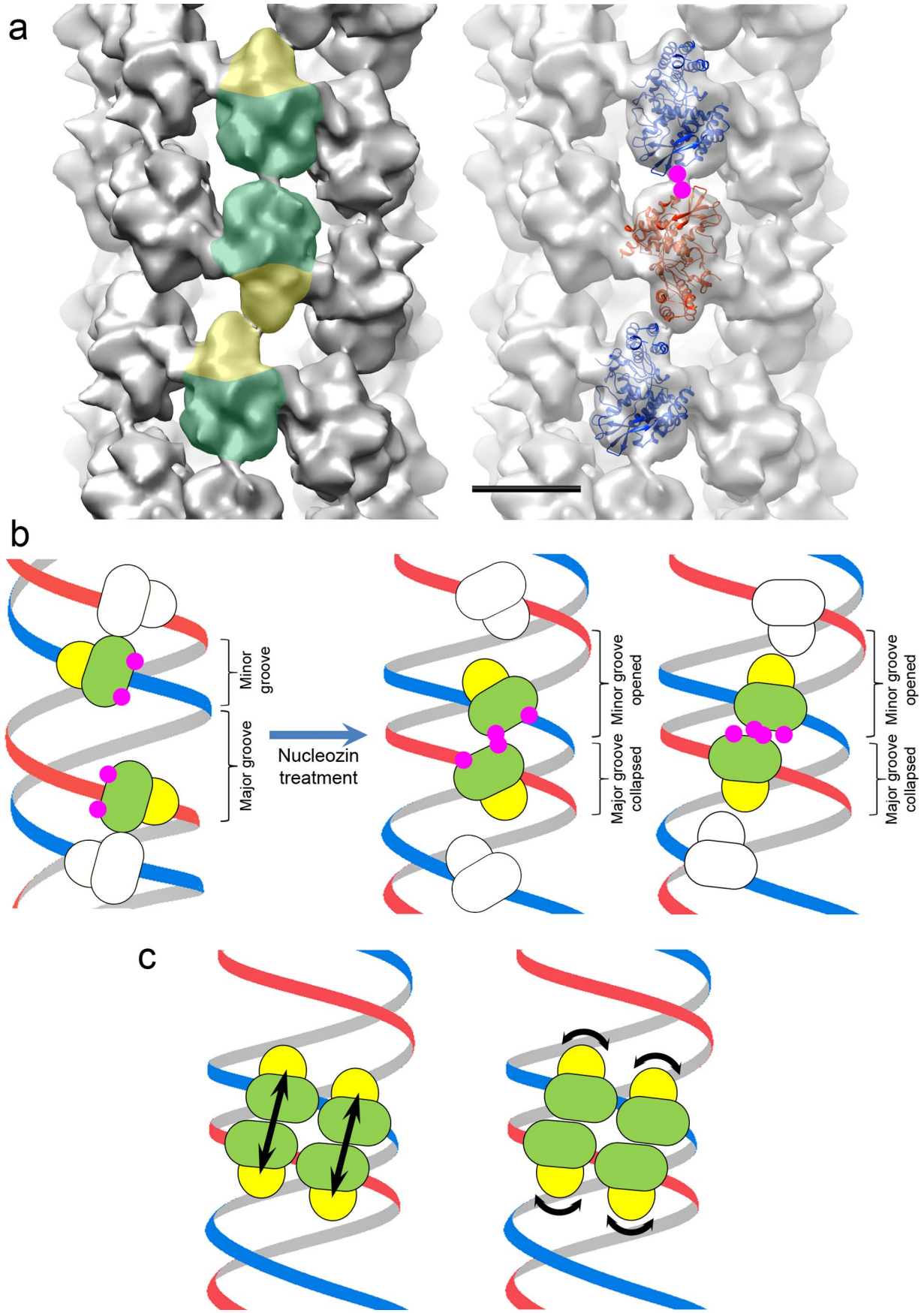

Extended Data Fig. 5 | See next page for caption.

Extended Data Fig. 5 | Effect of nucleozin on vRNP structure. a, Another structure obtained by cryo-EM after incubation of native vRNPs in the presence of nucleozin; the nucleozin binding site is marked with magenta circles. The structural changes are manifested in a decrease of z-rise, from 28–35 Å in untreated vRNPs to approximately 20 Å in the treated ones. Additionally, the phi angle drops from about 55–60 degrees to around 20 degrees. In consequence, the diameter of the helix increases (compare Fig. 3c and Extended Data Fig. 5a with Fig. 1a–d) and the vRNPs become shorter. Scale bar represents 50 Å. **b**, Scheme of the collapse of the major groove upon nucleozin treatment. On the left side, a draft of the wild type vRNP structure is shown, the upper (red) and lower (blue) strands and two pairs of nucleoproteins have been outlined, indicating the position of the nucleozin binding sites (magenta circles). In most cases, nucleozin probably binds to one nucleoprotein and the flexibility of the helix allows contact with the neighboring nucleoprotein of the contiguous turn, which produces the cross-linkage of both nucleoproteins, collapsing the major groove of the structure and opening the minor one. The right side of this panel shows two schemes for the helix after nucleozin binding corresponding to the structures shown in Fig. 3c and Extended Data Fig. 5a, respectively. **c**, Despite the cross-linking produced by nucleozin, vRNPs retain their flexibility due to the possibility of small movements among nucleoprotein dimers along the z-axis (left) or residual ability of the monomers to rotate (right). In this scheme, the nucleozin binding sites have been removed for clarity.

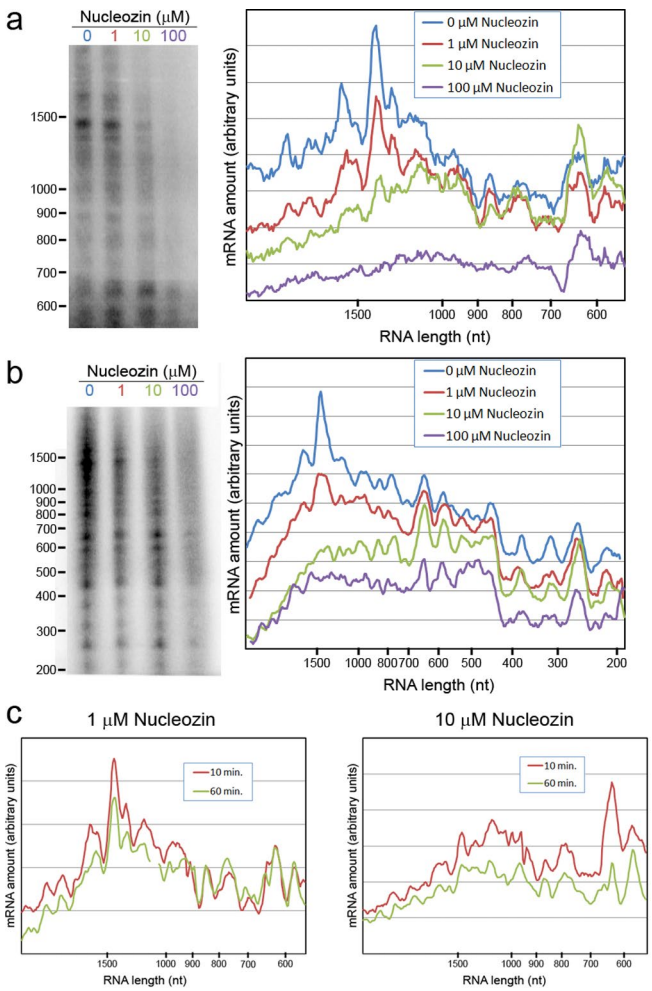

Extended Data Fig. 6 | Decreased *in vitro* transcriptional activity of vRNPs pre-incubated with nucleozin. a, Gel and quantification of mRNA synthesized in 1 h of transcription after 10 min of incubation with different concentrations of nucleozin. **b**, Gel and quantification of the shorter mRNAs synthesized in 1 h of transcription after 10 min of incubation with different concentrations of nucleozin. **c**, Effect of duration of nucleozin pre-incubation on mRNA synthesis by vRNPs. For treatments with small amounts of nucleozin (left panel, 1μM), the pre-treatment time had little influence on activity, but again affected longer mRNAs to a greater extent. One result of three independent experiments is shown.

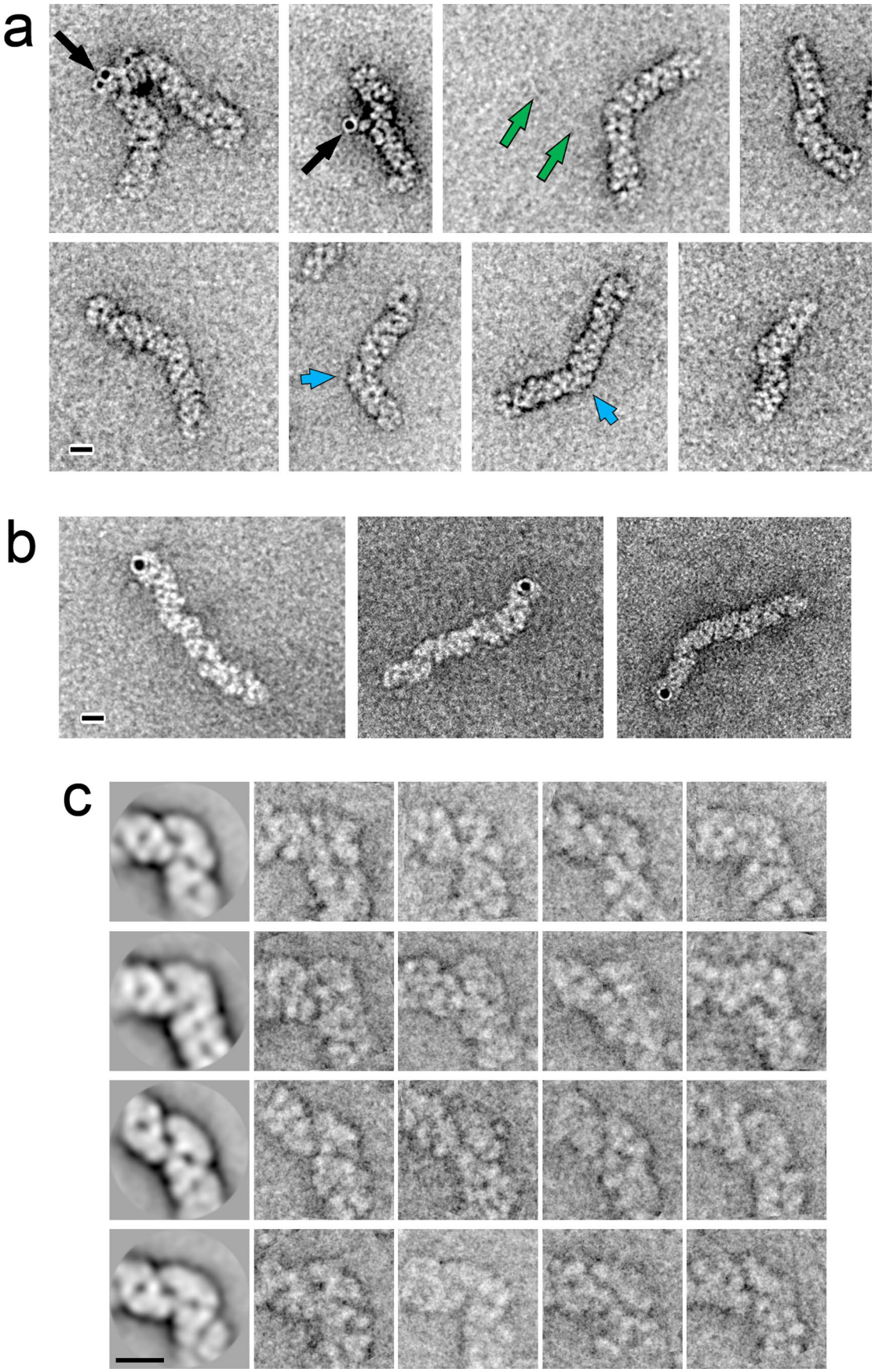

Extended Data Fig. 7 | See next page for caption.

Extended Data Fig. 7 | Electron microscopy of vRNPs during transcription. a, Image gallery of negatively stained vRNPs during the transcription process. In all cases a nucleoprotein loop is clearly visible at each end of the vRNP and the polymerase is located at some point along the helical part (blue arrows). The first two images show vRNPs where the His-tagged PB2 polymerase has been labeled with 5-nm Ni-NTA-Nanogold nanoprobe (black arrows). In some cases, an mRNA thread emerging from the polymerase was visible (green arrows). **b**, Gallery of non-activated control vRNPs showing the polymerase Ni-NTA-Nanogold labeled at one end. **c**, Average images obtained after alignment and classification of the region where the polymerase was located on the vRNPs during transcription. Each average was obtained from around 200 images; representative single images of the classes are shown on the right. Scale bars represent 150 Å.

Corresponding author(s): Juan Ortín
Jaime Martín-Benito

Reporting Summary

Nature Research wishes to improve the reproducibility of the work that we publish. This form provides structure for consistency and transparency in reporting. For further information on Nature Research policies, see Authors & Referees and the Editorial Policy Checklist.

Statistical parameters

When statistical analyses are reported, confirm that the following items are present in the relevant location (e.g. figure legend, table legend, main text, or Methods section).

n/a	Confirmed	
☒	☐	The exact sample size (*n*) for each experimental group/condition, given as a discrete number and unit of measurement
☒	☐	An indication of whether measurements were taken from distinct samples or whether the same sample was measured repeatedly
☒	☐	The statistical test(s) used AND whether they are one- or two-sided *Only common tests should be described solely by name; describe more complex techniques in the Methods section.*
☒	☐	A description of all covariates tested
☒	☐	A description of any assumptions or corrections, such as tests of normality and adjustment for multiple comparisons
☒	☐	A full description of the statistics including central tendency (e.g. means) or other basic estimates (e.g. regression coefficient) AND variation (e.g. standard deviation) or associated estimates of uncertainty (e.g. confidence intervals)
☒	☐	For null hypothesis testing, the test statistic (e.g. *F*, *t*, *r*) with confidence intervals, effect sizes, degrees of freedom and *P* value noted *Give P values as exact values whenever suitable.*
☒	☐	For Bayesian analysis, information on the choice of priors and Markov chain Monte Carlo settings
☒	☐	For hierarchical and complex designs, identification of the appropriate level for tests and full reporting of outcomes
☒	☐	Estimates of effect sizes (e.g. Cohen's *d*, Pearson's *r*), indicating how they were calculated
☒	☐	Clearly defined error bars *State explicitly what error bars represent (e.g. SD, SE, CI)*

Our web collection on statistics for biologists may be useful.

Software and code

Policy information about availability of computer code

Data collection	EPU software (ver 1.7.1, FEI company), SerialEM (ver 3.6.0 Beta)
Data analysis	Relion (ver 2.0), Scipion (ver 1.2), Xmipp (ver 3.0), Motioncorr (ver 2.1), CTFFIND (ver 4.1.1), Spider (ver 18.0), ImageJ (ver 1.42g).

For manuscripts utilizing custom algorithms or software that are central to the research but not yet described in published literature, software must be made available to editors/reviewers upon request. We strongly encourage code deposition in a community repository (e.g. GitHub). See the Nature Research guidelines for submitting code & software for further information.

Data

Policy information about availability of data

All manuscripts must include a data availability statement. This statement should provide the following information, where applicable:

- Accession codes, unique identifiers, or web links for publicly available datasets
  EMD-0175, EMD-4412, EMD-4423, EMD-4426 and EMD-4430 and pdb accession codes 6H9G, 6I54, 6I7B, 6I7M and 6I85
- A list of figures that have associated raw data
- A description of any restrictions on data availability: Volumes and docking of atomic structures are deposited in EMDataBank

Field-specific reporting

Please select the best fit for your research. If you are not sure, read the appropriate sections before making your selection.

☒ Life sciences ☐ Behavioural & social sciences ☐ Ecological, evolutionary & environmental sciences

For a reference copy of the document with all sections, see nature.com/authors/policies/ReportingSummary-flat.pdf

Life sciences study design

All studies must disclose on these points even when the disclosure is negative.

Sample size	The size of the ribonucleoproteins was theoretically calculated by adding the molecular weight of their isolated components plus RNA
Data exclusions	No data excluded from the analyses
Replication	All attemps of replication were successful
Randomization	Randomization is not relevant in this work
Blinding	Blinding is not relevant in structure determination

Reporting for specific materials, systems and methods

Materials & experimental systems

n/a	Involved in the study
☒	☐ Unique biological materials
☒	☐ Antibodies
☐	☒ Eukaryotic cell lines
☒	☐ Palaeontology
☒	☐ Animals and other organisms
☒	☐ Human research participants

Methods

n/a	Involved in the study
☒	☐ ChIP-seq
☒	☐ Flow cytometry
☒	☐ MRI-based neuroimaging

Eukaryotic cell lines

Policy information about cell lines

Cell line source(s)	MDCK (PTA-6500) and COS1 (CRL-1650) cell lines were obtained from the American Type Culture Collection. 293T cells were provided by the laboratory of Dr. Michel Perricaudet, Institut Gustave Roussy (Villejuif, France).
Authentication	Cell lines were not authenticated
Mycoplasma contamination	Cell lines were regularly tested for the presence of mycoplasma using the Myco-Alert Kit (Lonza).
Commonly misidentified lines (See ICLAC register)	In this study there is not any misidentified cell line